Aerodynamic and production comparison of wind farms with downwind versus conventional upwind turbines

Journal of Physics: Conference Series **2767** (2024) 092008 doi:10.1088/1742-6596/2767/9/092008

Aerodynamic and production comparison of wind farms with downwind versus conventional upwind turbines

Cory Frontin, Ganesh Vijayakumar, Pietro Bortolotti

National Wind Technology Center, National Renewable Energy Laboratory, Golden CO USA

E-mail: cory.frontin@nrel.gov, ganesh.vijayakumar@nrel.gov, pietro.bortolotti@nrel.gov

Abstract.

Ever-increasing turbine scales and their associated logistical challenges have reignited questions about the performance of downwind rotor configurations. A particular potential benefit of downwind rotor configurations is the farm-scale power increase that may be conferred by tilt-driven downward wake entrainment and associated wake recovery. In this work, a comprehensive aerodynamic analysis is carried out to understand the mechanisms for wake entrainment and recovery across a spectrum of velocity and inflow alignment conditions on a small, structured farm in order to understand the impact of downwind rotors on farm production. The results show that the benefits demonstrated previously in the literature for downwind-rotor farms in aligned flows are fragile, and, outside of strong farm/flow alignment conditions, power production benefits for small farms with downwind rotor configurations are significantly if not completely mitigated by misalignment effects. The work indicates that farm-scale benefits for downwind rotors must be realized either from large-scale entrainment benefits, with more exotic farm arrangements that can take advantage of the aerodynamic effects, or from beneficial fatigue impacts from entrainment of less turbulent outer boundary layer flows.

1 Introduction

The interaction between a wind turbine and the downstream farm flow is dominated by the turbine's wake: the variation of the flow downstream of the turbine with respect to the otherwise undisturbed flow [1]. Early attention to farm flow was concentrated on the diversion of wakes away from downstream turbines, which can be effectuated by deflecting the yaw of a turbine out of the freestream direction [2]. Recently, more attention has been paid to the tilt angle of the turbine, where the turbine hub is rotated about the axis in the horizontal plane and perpendicular to the hub shaft. The majority of present-day rotor designs have the rotor upstream of the tower to avoid tower shadow losses [3] and noise [4] that occur when the rotor interacts with tower-perturbed flow; in this case, the tilt angle is typically set to avoid tower strike when the blades deflect. The historical development of wind turbines has included both upwind rotor (UWR) and downwind rotor (DWR) designs, although the UWR configuration has consistently been the dominant configuration. However, recent work has reopened longstanding questions about the contemporary preference for land-based wind turbines with upwind, rather than downwind, rotor configurations for logistical, structural, and aerodynamic reasons [5].

The potential aerodynamic benefits of downwind rotor configurations are driven by the tilt angle: UWR configurations displace the lower tip of the rotor into the upstream flow, which tends to induce upward wake flow. On the other hand, DWR tilt angles do the opposite and induce downward wake flow. In Figure 1, the geometries are compared, with a qualitative representation of their vertical wake

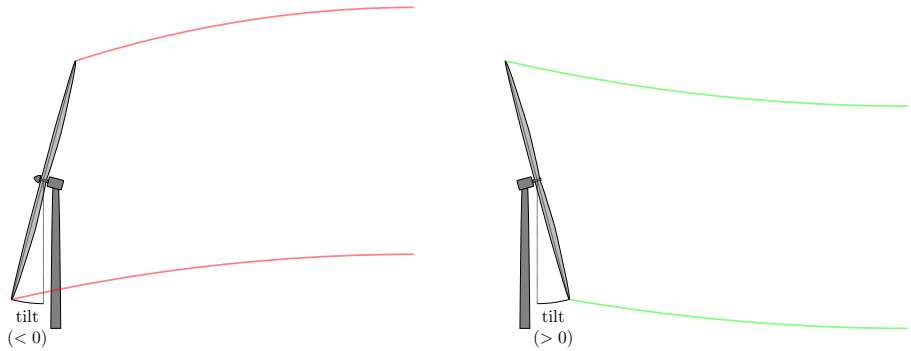

Figure 1: Comparison of upwind rotor (left, with negative tilt) vs. downwind rotor (right, with positive tilt) and their qualitative effects on the vertical wake motion. Freestream from left.

redistribution. Off-optimal tilt angles tend to decrease the power output of a turbine in isolation, but on the farm scale the downward displacement of the wake with DWR configurations can entrain smooth (i.e., less turbulent), momentum-rich flow from the outer boundary layer for ingestion by the next rows. This effect has been robustly demonstrated in simulation for a single turbine [6] as well as for a two-turbine dyad [7]. Those results informed studies using engineering wake models [8], which allowed estimates of the impact of reversing a subset of turbines on the farm-scale aerodynamics.
Recently, these estimates have since been refined by high-fidelity farm-scale studies, which have demonstrated with actuator-disk large-eddy simulation (LES) that the use of high-tilt DWR configurations can result in significant farm-scale power gains at fixed, favorable farm alignment and inflow velocity [9]. It has been postulated that these gains are analogous to naturally occurring aerodynamic modes in canonical turbulent flows [10]; this suggests power improvements may be highly sensitive to farm configuration and prevailing conditions.
In this work, high-fidelity estimates of land-based farm flow are generated across a spectrum of conditions to understand the effect of transitioning from traditional UWR configurations to DWR configurations on turbine- and farm-scale aerodynamics. The goal is to understand how farm-scale aerodynamic effects can be anticipated to impact farm annual energy production (AEP) and suggest paths toward more comprehensive understanding of the benefits or lack thereof of UWR-configured farms.

2 Numerical experiment

To study the farm-scale aerodynamics, we simulate a neutral atmospheric boundary layer (ABL) over land with a prescribed capping inversion at 700 m (applied using a 0.08°C/m capping gradient and 0.003°C/m upper temperature gradient). The neutral boundary layer is chosen in order to conform with the existing literature and to give an intermediate result compared to the stable and unstable ABLs. The simulation is located at 40°N latitude with sea level standard atmospheric properties (1.225 kg/m^3 density, 1.0×10^{-5} kg/(m·s) viscosity, and a reference temperature of 290 K). The simulation is carried out using the `amr-wind` wall-modeled LES solver [11], with the solver's standard log-law wall model and the Moeng subgrid-scale model [12]. The domain for the simulation consists of a 12 km square domain with a 1200 m ceiling.

2.1 Precursor simulations

Precursor simulations are run to establish baseline ABL flow. Each simulation is run to target a freestream hub-height velocity $U_{\infty,\text{hub}}$, always aligned with the x-coordinate in the mesh frame of reference. The forcing pressure gradient is controlled to achieve the intended $U_{\infty,\text{hub}}$ as the simulation is run from time $t = 0$ to $t = 25 \times 10^3$ s, such that the mean hub-height velocity converges satisfactorily to the intended $U_{\infty,\text{hub}}$ by $t = 22 \times 10^3$ s. Simulations are run with a time step $\Delta t = 0.5$ s and a uniform grid of $N_{\text{elem}} = 75$M total elements ($768 \times 768 \times 128$ in the streamwise, spanwise, and vertical directions, respectively). The wall-model boundary condition is applied at the floor at $z = 0$, and a slip wall boundary is applied at the ceiling, with periodic boundaries in x and y. The solutions from these precursor simulations are used as initial conditions and boundary conditions for the forthcoming farm simulations.

2.2 Farm simulations

Farms are simulated using an immersed actuator line method that uses coupling to the aeroservoelastic framework OpenFAST [13]. The farm consists of a 4×4 square grid, centered in the domain and with $6D_{\text{rotor}}$ spacing, where D_{rotor} is the diameter of the rotor. Turbines are taken from the Big Adaptive Rotor (BAR) project [14] and have a D_{rotor} of 206 m, hub height of 140 m, and a rating of 5 MW. The design of the rotor within the BAR project aimed to relax stiffness requirements typically seen in contemporary rotor design and represent blades which are poised to exploit the DWR configuration in particular. Columns of the farm are rotated with respect to the freestream velocity (and, therefore, the x-coordinate in the mesh frame of reference) by an inflow angle ψ. In the farm simulation, the initial farm condition at $t = 22 \times 10^3$ s and the upstream boundary condition in x are set to the values from the relevant precursor simulation; the downstream boundary in x is an outflow boundary, and the domain remains periodic in y. Two courses of isotropic grid refinement are applied, centered on towers and extending out from the center of the tower by D_{rotor}, giving $N_{\text{elem}} \approx 90$M total elements; the time step for the farm simulation is run more finely than the precursor at $\Delta t = 0.1$ s, and precursor solutions are interpolated into the fine temporal grid by `amr-wind`.

2.3 Experimental outputs

The results of the simulations in this work take a threefold approach to analyze the impact of DWR configurations on the aerodynamic flows. First, OpenFAST output signals from the actuator-line turbine models are used to analyze the generator power outputs in a given simulation case, allowing analysis on a farm-scale basis as well as on a turbine-by-turbine basis.

Additionally, aerodynamic flows on the farm scale are studied by control-volume analyses to understand the bulk flow of momentum into the relevant—i.e., extractable—rotor area. We are interested in the flow into and out of the region from which turbines might extract momentum as power. We take the extraction region to be the region under the plane defined by the upper extrema of the turbine rotors:

$$\Omega_{\text{ext}} \equiv \{\mathbf{x} \in \Omega \,|\, z \leq z_{\text{tip}}\}\,, \tag{1}$$

where Ω is the computational domain and $z_{\text{tip}} = h_{\text{hub}} + \frac{1}{2}D_{\text{rotor}}$. The result of integrating the momentum equation on the Ω_{ext} gives

$$\frac{\mathrm{d}}{\mathrm{d}t}\left(\int_{\Omega_{\text{ext}}} \rho u_i \,\mathrm{d}\Omega\right) = -\int_{\partial\Omega_{\text{ext}}} (\rho u_i u_j)\cdot \hat{n}_j \,\mathrm{d}\Gamma + \ldots, \tag{2}$$

where the volume terms are withheld. The flux of momentum $\rho u_i u_j$ represents, then, the instantaneous momentum flow into and out of Ω_{ext} through its boundaries. In this work we will consider only the "bulk" momentum flux—that involving only the mean flow:

$$\bar{\mathcal{F}}_{\text{mom},ij} = \rho \bar{u}_i \bar{u}_j. \tag{3}$$

This quantity is measured along the horizontal plane at $z = z_{\text{tip}}$ with $x_j = z$, giving the flux of momentum through the tip plane, thus quantifying the entrainment of momentum into the region from which it can be extracted.

Lastly, the turbine-by-turbine flows are analyzed. To do so, virtual (nonintrusive) meteorological tower ("met tower") measurements are taken $D_{\text{rotor}}/2$ upstream of the tower location to isolate the measured quantities from the turbine induction and allow fair comparison between UWR and DWR configurations. These towers allow time-resolved storage of the velocities along the vertical towers, $\mathbf{u}_{\text{met}}(z,t)$, from which mean velocity profiles, $\bar{\mathbf{u}}_{\text{met}}(z)$, are computed. Finally, in order to understand how changes to velocity of ingested flow change the power that can be extracted from a fluid, we make an estimate of the linear density of power on the rotor, $P'_{\text{fluid}}(z)$, as defined by:

$$P'_{\text{fluid}}(z) = \frac{1}{2}\rho A'_{\text{rotor}}(z)\, \bar{u}^3_{\text{met}}(z). \tag{4}$$

Using $\bar{u}_{\text{met}}(z)$ here represents an approximation, assuming that $\bar{u}_{\text{met}}(z)$ well approximates the mean flow across the slice $A'_{\text{rotor}}(z)$ of the rotor plane. Assuming this approximation holds, $P_{\text{fluid}} = \int_z P'_{\text{fluid}}(z)\,\mathrm{d}z$, and $P'_{\text{fluid}}(z)$ will represent the distribution of fluid power available for conversion across the vertical profile of the rotor.

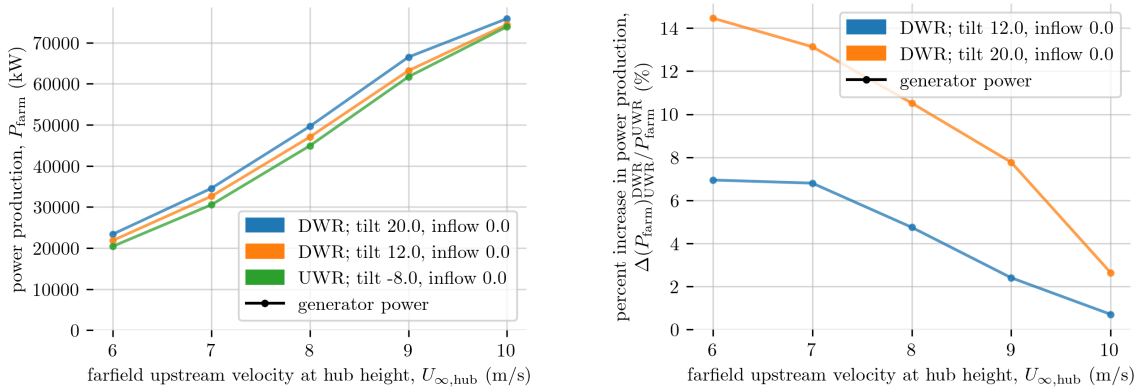

Figure 2: Comparison between power production by UWR farm and DWR farms at varied tilt angles for freestream-aligned farms. Power averaged over final 20 minutes of simulation. Percent comparison benchmarked to $-8°$ tilt UWR farm.

3 Results for freestream-aligned farm

3.1 Power production at the farm scale

First, the power production of a wind farm with the inflow angle aligned with the farm columns ($\psi = 0$) is considered. Simulations have been run with $U_{\infty,\text{hub}}$ between 6 m/s and 10 m/s and for farms with a UWR configuration at $-8°$ of tilt and DWR configurations at $+12°$ and $+20°$ of tilt. These tilt angles are chosen to represent a conservative and aggressive choice that are, on the conservative side, substantial enough to deflect the wakes, while on the aggressive side representing large but plausible tilt angles.. The result of this study is shown in Figure 2, which shows that power improvements exist across the velocity spectrum for the aligned DWR configuration farms. The percent improvement for the $+20°$ tilt DWR farms are in excess of 8% for all velocities below approximately 9 m/s; at 10 m/s, all three farms are rapidly approaching saturation at the plant's nameplate capacity of 80 MW, and the improvement in the DWR farms falls off correspondingly.

3.2 Power production at the turbine scale

Next, the turbine-by-turbine power production is considered. We concentrate on the case that generates the largest absolute improvement in power, with $U_{\infty,\text{hub}} = 9$ m/s and $+20°$ of tilt. In Figure 3, the turbine-by-turbine breakdown of the performance is shown. The first row of turbines suffers a small power loss, around half a percent, due to misalignment with the inflow. On the second row, the losses are reversed, and the second row of DWR turbines all generate between 2% and 7% increases in power compared to the UWR benchmark case; the third and fourth rows exhibit significant increases in power. We note that there exists significant column-to-column variation within each row, due to wind veer and statistical averaging effects. Our computational runs were budgeted to have sampling time in excess of the standard ten-minute averaging in the literature. Across the velocity spectrum, results have similar qualititative behavior row-by-row, and consistent farm averages, allowing us to remain confident that the farm-averaged effects can be used to draw valid conclusions about the UWR vs. DWR differences.

3.3 Aerodynamic flows at the farm scale

To understand the power improvement observed in the previous section, the farm-scale flows are now visualized. In Figure 4, the bulk momentum flux defined in Equation 3 is shown. We compare the $-8°$ tilt UWR farm to the $+20°$ DWR farm; the comparison highlights the significant increase in bulk momentum flux through the tip plane in the DWR wake. This flux represents momentum being entrained into the wake regions, a less-turbulent, momentum-rich flow from the outer boundary layer. In addition to the downward entrainment in the DWR case, there is also increased flux out of the harvestable domain (in red) in between the columns of the farm. Effectively, the DWR-configured rotor creates a vortical structure in the wake of the aligned farm, which conforms to previous findings of Cossu [9, 10]. In Section 4, we will return to this behavior and consider its stability in the case of farm misalignment.

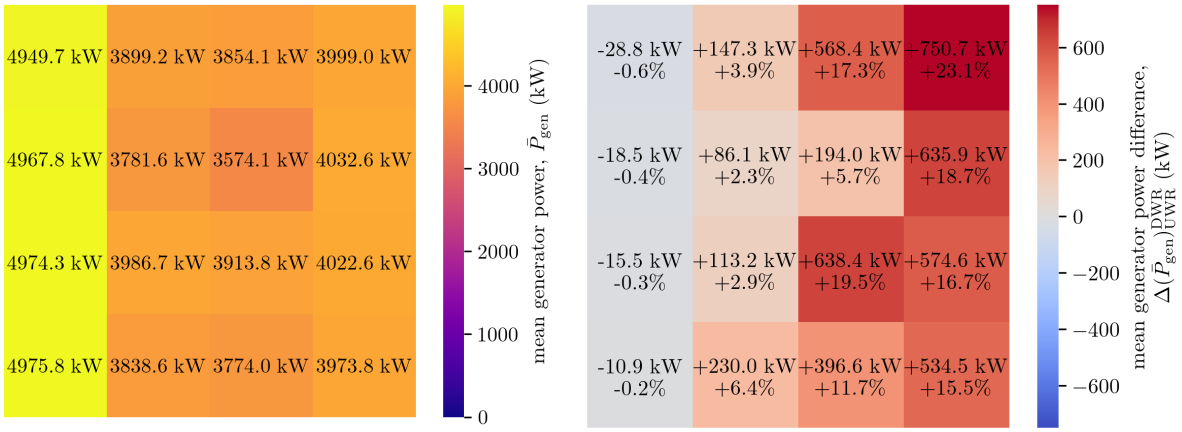

Figure 3: Turbine-by-turbine power generation and change in power for +20° tilt DWR turbine. Power averaged over final 20 minutes of simulation. White squares indicate zero change in power, red indicates increased power for DWR turbine, and blue indicates decreased power for DWR turbine compared to benchmark case. Comparison benchmarked to −8° tilt UWR farm. Farm inflow aligned with columns, from left on page.

3.4 Aerodynamic flows at the turbine scale

Before considering the misaligned farm, the impact of entrainment at the turbine scale is analyzed using the virtual met tower data. In Figure 5, the results can be found, again for the 9 m/s case. On the front row, differences are negligible and due exclusively to differences in the induction. On the second row, changes to the velocity profile are concentrated on the upper half of the rotor, where the velocity sees a significant increase. On the lower half of the rotor, there can exist a velocity deficit, but the magnitude of the deficit is less than the velocity augmentation on the upper half. The upwind rotors with +20° tilt also have less spread in velocity on the top half of the rotor, indicating lower turbulence intensity and– therefore– smoother flow.

A more meaningful measure of the impact to the power production is realized in the time-averaged linear density of fluid power, $P'_{\text{fluid}}(z)$ as defined in Equation 4, on the rotor, displayed in Figure 6. This metric shows that the entrainment of momentum into the wakes exposes a turbine in the wake of a DWR to higher and more imbalanced fluid power compared to the traditional UWR configuration.

4 Results for freestream-misaligned farm

Having demonstrated power benefits of the DWR-configured farms across the distribution of farm-aligned wind velocities, the impact of DWR-configured farms is now considered across a distribution of wind directions to begin to understand the impact DWR configurations might have on farm AEP. Here, we will concentrate on a fixed wind speed of 6 m/s, at which the highest percent improvement occurs in the aligned case.

4.1 Power production

The finding of Figure 2 is now revisited to understand variations with respect to the angle of alignment. In Figure 7, the percent change in power as a function of inflow angle[1] is shown for two DWR configurations at 6 m/s as benchmarked against the 8°-tilt UWR turbine. Unlike in the aligned case, power benefits are isolated to 0°, 45°, and approximately ±25°. These angles are significant, representing slope ratios of 0:1, 1:1, and approximately 2:1, which correspond directly to the angles at which turbine pairs in the farm are aligned with respect to the freestream. Turbine-by-turbine breakouts are omitted for the misaligned flow, but we note that the power deficits on waked rows are higher percentages than the first row, suggesting adverse aerodynamic effects, not just geometric effects.

[1]The study in this work includes the range of inflow angles from 0 to 45°, which would fully characterize a farm with this geometry in the absence of veer. We also includes the range from −25° to 0° to evaluate the impact of veer-induced asymmetry at 40°N latitude. For computational savings and in the absence of farm-scale benefits from DWR rotors, inflow angles were not extended further to compete the characterization of the farm.

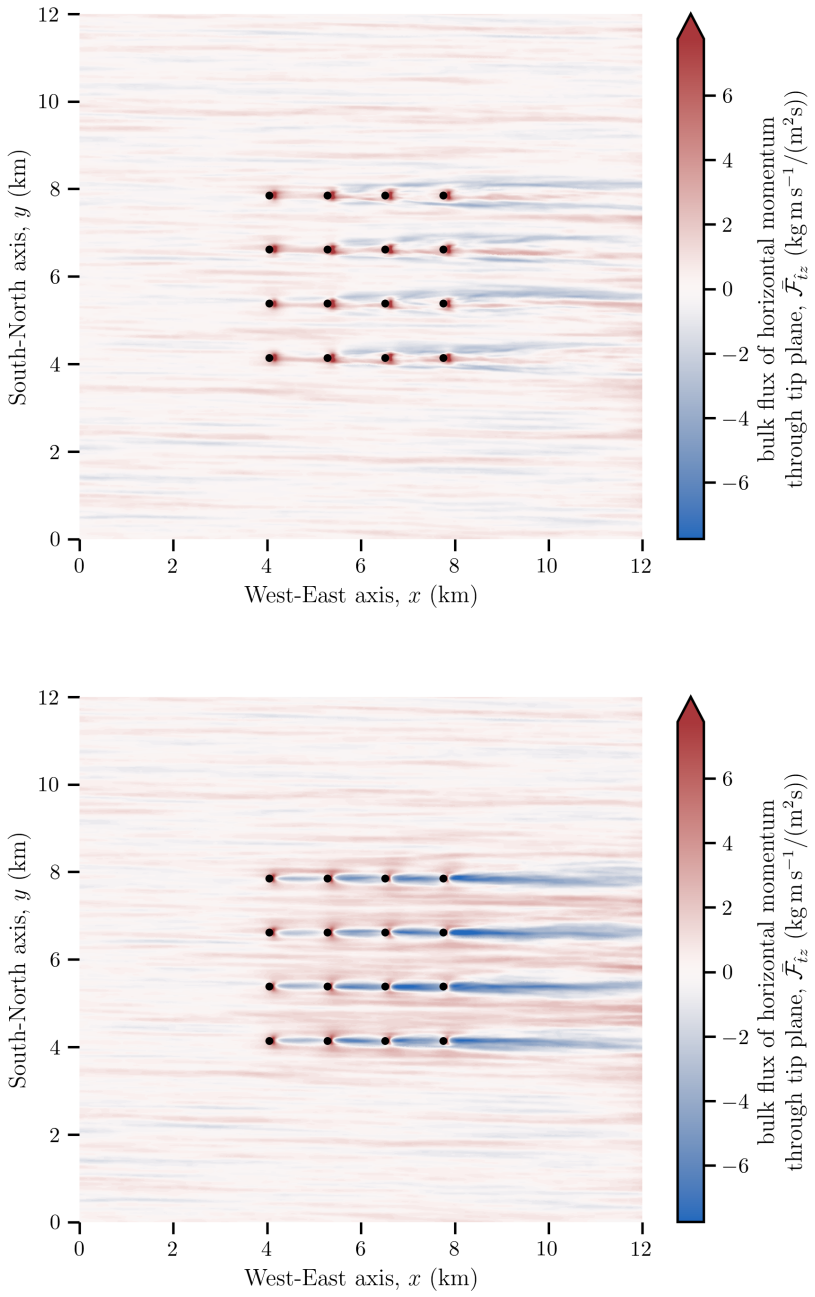

Figure 4: Bulk momentum flux $\bar{\mathcal{F}}_{\mathrm{mom},ij}$ for $-8°$ tilt UWR farm (upper) and $+20°$ tilt DWR farm (lower) through tip plane at $z = z_{\mathrm{tip}}$. Flow averaged over final 20 minutes of simulation. White regions indicate zero flux through tip plane, red indicates bulk momentum flux out of harvestable region, and blue indicates flux into harvestable region; colormaps matched between plots, values that exceed colorbar scale exist only in immediate vicinity of blades. Farm inflow aligned with columns, from left on page.

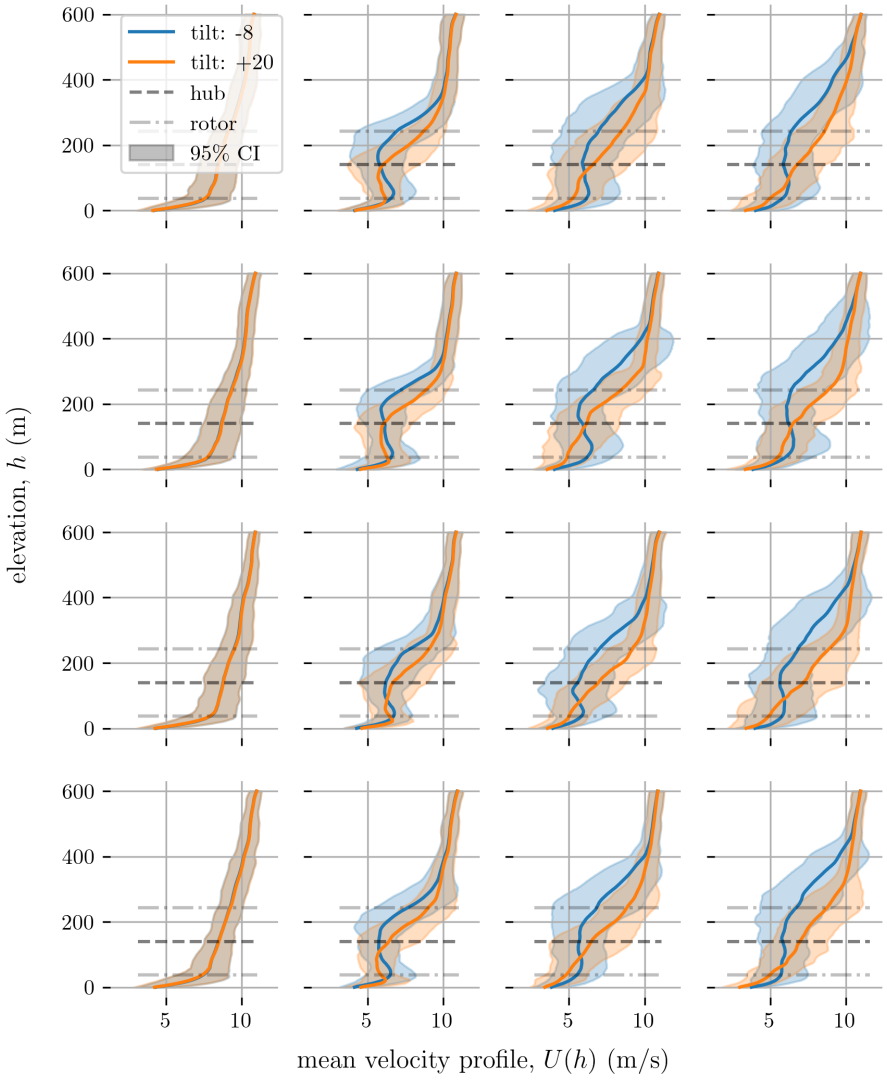

Figure 5: Comparison of turbine-by-turbine velocity profiles for $-8°$ tilt UWR turbine and $+20°$ tilt DWR turbine. Velocity averaged over final 20 minutes of simulation. Shading represents two standard deviations ($\sim 95\%$ confidence intervals). Farm inflow aligned with columns, from left on page.

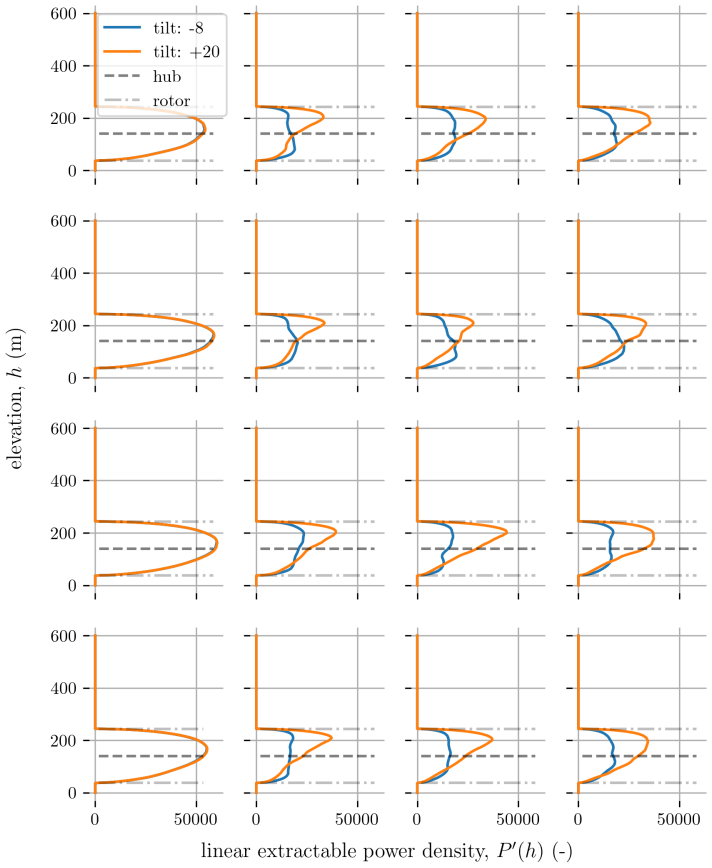

Figure 6: Comparison of turbine-by-turbine linear fluid power density profiles for $-8°$ tilt UWR turbine and $+20°$ tilt DWR turbine. Power density profiles averaged over final 20 minutes of simulation. Farm inflow aligned with columns, from left on page.

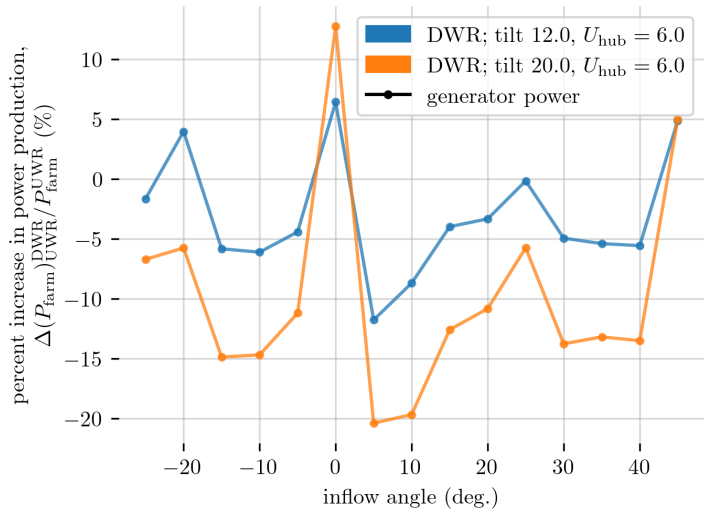

Figure 7: Comparison between power production by UWR farm and DWR farms at varied tilt angles for farms at $U_{\infty,\text{hub}}$ of 6 m/s. Power averaged over final 20 minutes of simulation. Percent comparison benchmarked to $-8°$ tilt UWR farm.

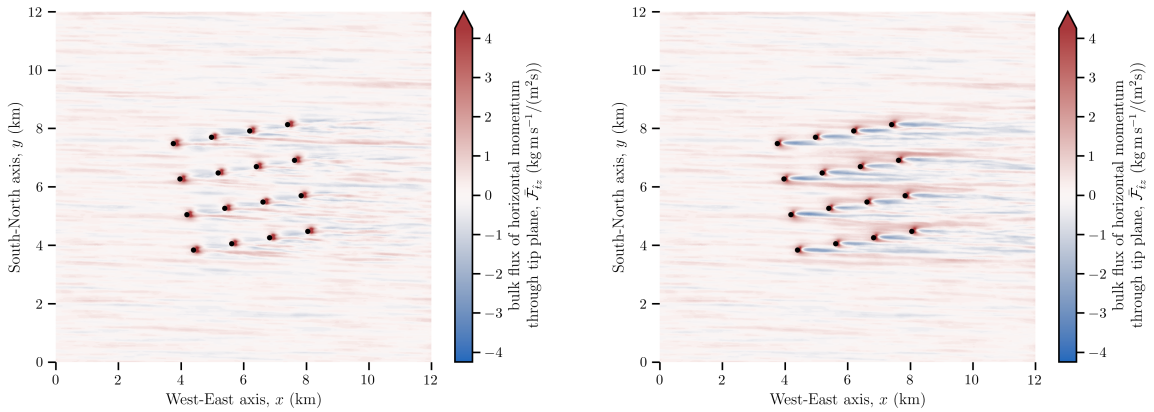

Figure 8: Bulk momentum flux $\bar{\mathcal{F}}_{\text{mom},ij}$ for $-8°$ tilt UWR farm (left) and $+20°$ tilt DWR farm (right) through tip plane at $z = z_{\text{tip}}$ at $U_{\infty,\text{hub}}$ of 6 m/s. Flow averaged over final 20 minutes of simulation. White regions indicate zero flux through tip plane, red indicates bulk momentum flux out of harvestable region, and blue indicates flux into harvestable region; colormaps matched between plots, values that exceed colorbar scale exist only in immediate vicinity of blades. Farm inflow corresponds with x-axis on plot from west on plot; inflow is offset from columns by $10°$ inflow angle.

4.2 Aerodynamic flows at the farm scale

In Figure 8, the bulk momentum flux $\bar{\mathcal{F}}_{\text{mom},ij}$ for the $10°$ inflow angle farm is shown, where entrainment by the DWR-configured farm is evident, as it was in Figure 4. However, due to the offset angle, turbines in downstream rows are not exposed to momentum-rich flow in the direct wake of turbines; rather, they are exposed to the flow between farm columns, which is momentum-deficient because surface-level fluid is displaced into the streets between rows.

Figure 8 also shows that the DWR-configured farm has a more active and structured wake downstream of the farm, with significant regions of net convective flux of momentum into the harvestable region. The limitations of this set of experiments also become apparent: the effects on this small farm may not capture the mixing effect of the momentum flux that may accumulate on a large farm or in other ABL conditions. It is possible that for a larger farm, the increased turbine wake intersections—in addition to farm-scale mixing and momentum entrainment effects—may result in wake recovery performance and AEP benefits for DWR farms.

5 Conclusion

In this work, the performance of farms with downwind rotor turbines has been compared to the traditional farm of upwind rotor turbines using actuator-line LES studies. Studies of the aligned farm performed in this work confirm the benefits for freestream-aligned farms previously demonstrated in the literature and contribute detailed descriptions of the increase in momentum and fluid power available for the turbines in the farm that are subject to wake effects. Our findings show that the power benefits due to entrainment that occur for small, aligned farms of downwind rotors are not present when there is even small misalignment of the columns of the farm with respect to the freestream flow. These losses exceed those expected due to geometric changes alone and indicate that the DWR configuration causes waked turbines to ingest momentum-deficient flow when the farm is misaligned.

As a whole, these results cast uncertainty on the utility of fully downwind-configured farms. Though we stop short of a fully specified AEP calculation, our results demonstrate the collapse of benefits for all but a very small region in the wind rose for this experiment, for which few realistic wind distributions might give a net AEP benefit. A key outstanding question is whether the losses that we anticipate this experiment's small, structured farms persist as farm scale and complexity increase. One item for further study is a larger farm, which can concentrate on the worst-case misalignment, to reveal if large-scale effects recover power (and therefore AEP) benefits across a range of inflow conditions.

In addition to the studies shown here, which focus exclusively on power extraction, fatigue and lifetime cost considerations should also be made. As shown in Figure 6, the downwind rotor configuration

increases imbalance of loading about the hub. Moreover, in the process of the analysis—though the results are not shown explicitly in the scope of this manuscript—the turbulence intensity across the rotor are revealed to be less intense in the case of the downwind configuration; this occurs because the entrained flow from the upper region of the boundary layer is more smooth than near-surface flows. In future work, the aerodynamic and structural model data generated for this study can be used for a more complete view of the downwind-configuration farm, including structural trade-offs with the changes in power.

Acknowledgments
The authors would like to thank Luis A. "Tony" Martínez Tossas for assistance in configuring the LES studies in this work. The research in this manuscript was performed using computational resources sponsored by the Department of Energy's Office of Energy Efficiency and Renewable Energy and located at the National Renewable Energy Laboratory. This work was authored by the National Renewable Energy Laboratory, operated by Alliance for Sustainable Energy, LLC, for the U.S. Department of Energy (DOE) under Contract No. DE-AC36-08GO28308, with funding provided by the U.S. Department of Energy Office of Energy Efficiency and Renewable Energy Wind Energy Technologies Office. The views expressed in the article do not necessarily represent the views of the DOE or the U.S. Government. The U.S. Government retains and the publisher, by accepting the article for publication, acknowledges that the U.S. Government retains a nonexclusive, paid-up, irrevocable, worldwide license to publish or reproduce the published form of this work, or allow others to do so, for U.S. Government purposes.

References

[1] Porté-Agel F, Bastankhah M and Shamsoddin S 2020 *Boundary-Layer Meteorology* **174** 1–59

[2] Jiménez Á, Crespo A and Migoya E 2009 *Wind Energy* **13** 559–572

[3] Reiso M 2013 *The Tower Shadow Effect in Downwind Wind Turbines* Ph.D. thesis Norwegian University of Science and Technology Trondheim, Norway

[4] Kelley N, McKenna H, Hemphill R, Etter C, Garrelts R and Linn N 1985 Acoustic noise associated with the MOD-1 wind turbine: Its source, impact, and control Tech. Rep. SERI/TR-635-1166, 5875386 Solar Energy Research Institute

[5] Bortolotti P, Ivanov H, Johnson N, Barter G E, Veers P and Namura N 2022 *Wind Energy* **25** 354–367

[6] Fleming P A, Gebraad P M, Lee S, Van Wingerden J W, Johnson K, Churchfield M, Michalakes J, Spalart P and Moriarty P 2014 *Renewable Energy* **70** 211–218

[7] Fleming P, Gebraad P M, Lee S, Van Wingerden J W, Johnson K, Churchfield M, Michalakes J, Spalart P and Moriarty P 2015 *Wind Energy* **18** 2135–2143

[8] Bay C J, Annoni J, Martinez-Tossas L A, Pao L Y and Johnson K E 2019 *2019 American Control Conference (ACC)* (Philadelphia, PA, USA: IEEE) pp 2843–2848 ISBN 978-1-5386-7926-5

[9] Cossu C 2021 *Wind Energy Science* **6** 663–675

[10] Cossu C 2021 *Wind Energy* **24** 345–356

[11] Ananthan S, Brazell M, Rood J, Vijayakumar G, Henry de Frehan M, Almgren A, Zhang W and Sprague M 2020 AMR-Wind National Renewable Energy Laboratory, Lawrence Berkeley National Laboratory, Sandia National Laboratory

[12] Moeng C H 1984 *Journal of the Atmospheric Sciences* **41** 2052–2062

[13] Churchfield M, Lee S, Moriarty P, Martinez L, Leonardi S, Vijayakumar G and Brasseur J 2012 *50th AIAA Aerospace Sciences Meeting Including the New Horizons Forum and Aerospace Exposition* (Nashville, Tennessee: American Institute of Aeronautics and Astronautics) ISBN 978-1-60086-936-5

[14] Bortolotti P, Johnson N, Abbas N J, Anderson E, Camarena E and Paquette J 2021 *Wind Energy Science* **6** 1277–1290